Available online at www.sciencedirect.com
SCIENCE DIRECT®
Medical Image Analysis 10 (2006) 397–412
MEDICAL IMAGE ANALYSIS
www.elsevier.com/locate/media

Lagrangian frame diffeomorphic image registration: Morphometric comparison of human and chimpanzee cortex

Brian B. Avants *, P. Thomas Schoenemann, James C. Gee

Departments of Bioengineering, Radiology and Anthropology, University of Pennsylvania, Philadelphia, PA 19104-6389, United States

Received 30 September 2004; received in revised form 9 February 2005; accepted 4 March 2005
Available online 3 June 2005

Abstract

We develop a novel Lagrangian reference frame diffeomorphic image and landmark registration method. The algorithm uses the fixed Langrangian reference frame to define the map between coordinate systems, but also generates and stores the inverse map from the Eulerian to the Lagrangian frame. Computing both maps allows facile computation of both Eulerian and Langrangian quantities. We apply this algorithm to estimating a putative evolutionary change of coordinates between a population of chimpanzee and human cortices. Inter-species functional homologues fix the map explicitly, where they are known, while image similarities guide the alignment elsewhere. This map allows detailed study of the volumetric change between chimp and human cortex. Instead of basing the inter-species study on a single species atlas, we diffeomorphically connect the mean shape and intensity templates for each group. The human statistics then map diffeomorphically into the space of the chimpanzee cortex providing a comparison between species. The population statistics show a significant doubling of the relative prefrontal lobe size in humans, as compared to chimpanzees.

Keywords: Diffeomorphic; Deformable image registration; Primate cortex; Evolution; Morphometry

1. Introduction

The relationship between the primate and the human brain has intrigued researchers in evolution, biology and medicine since at least the 19th century (Huxley et al., 1874; Thompson, 1917) and remains an area of active research (Deacon, 1997; Schoenemann et al., 2004; Essen, 2004a). Understanding functional and anatomical inter-species correspondences is fundamental to connecting human and animal research. Chimpanzee language, disease and behavioral studies are often used as a starting point for understanding human medical conditions. These studies become more valuable as our ability to relate them to human subjects increases. Volumetric medical image registration permits one to make inter-species neuroanatomical comparisons between subjects by using known functional and structural constraints. Furthermore, diffeomorphic transformations (Miller et al., 2002) between species (Essen et al., 2001) may aid in understanding the evolutionary process.

Diffeomorphisms permit comparisons under the hypothesis that the topology of the deforming anatomy must be preserved. Transformations are differentiable and guaranteed to be one-to-one and onto: for every position in one image, there is a single corresponding position in the second image. These properties also mean that the transformations may be composed. If we have a transformation taking I to J and a transformation taking J to K, we also have both I to K and K to I through composition. The diffeomorphic framework also supplies a rigorous mathematical metric between anatomies, a valuable quantitative measure of the distance between images.

Landmarking is an invaluable tool for gaining anatomically correct image registrations in cases where

* Corresponding author.
E-mail address: avants@grasp.cis.upenn.edu (B.B. Avants).

1361-8415/$ - see front matter © 2005 Elsevier B.V. All rights reserved.
doi:10.1016/j.media.2005.03.005

noise, lack of features or pure anatomical complexity make automated methods unreliable (Thompson and Toga, 1998). Bookstein's point-based thin-plate splines revealed the power of this approach for studies of human and non-human shape variability (Bookstein, 1992). Previously, diffeomorphic image matching and diffeomorphic landmark matching were solved by independent algorithmic frameworks. Image matching solutions are found in the Eulerian domain in Miller and Christensen's work (Miller et al., 2002; Christensen et al., 1996), while landmark matching is solved in the Lagrangian domain by Joshi and Miller (2000) or with interpolating splines (Twining and Marsland, 2003). Our algorithm for diffeomorphic registration solves both the image and landmark matching problems in the Lagrangian reference frame, while generating the inverse transformation. This allows one to solve either landmark or image matching independently or to use a weighted combination of both image and landmark similarities. Landmarks are essential for making a meaningful connection between closely related species.

Historically, in situ research on primate brain anatomy and function was based on unethical treatment of captive animals. Current technology in magnetic resonance imaging (MRI) allow both the function and the structure of the brain to be non-invasively measured, in a humane environment, without direct detriment to the subject. Image-based research in this area is often focused on the surface view of the cortex (Essen et al., 1998), promoted by Van Essen. Surface-based methods focus on the basic computational structure of the brain: the thin, folded layer of gray matter. However, these methods ignore important internal structures, such as the ventricles, and must rely on topologically correct cortical surface segmentations (Han et al., 2003). Van Essen uses 12 (6 per hemisphere) functionally based anatomical landmarks to constrain inter-species surface deformations (Essen, 2004b) for an analysis of competing visual cortex partitionings. These landmarks map the domains such that one may visualize the relative deficit or surfeit of functional areas between species, as well as the relative topology of the functional regions (Essen, 2004a). In contrast, our study uses extant *volumetric and surface-based* knowledge of anatomical and functional similarities between the human and the chimpanzee cortex. These landmarks enable us to reverse-engineer a plausible topology preserving evolutionary transformation.

Our scientific goal is both to generate the evolutionary transformation and to study *volumetric* cortical chimp–human structural differences that it reveals. The study is based on MRI, diffeomorphic image registration and standard cortico-functional relationships between chimp and human anatomy. Between species functional homologues are held as constant across individuals and are used to guide structures of interest into alignment. The structural data on the cortex is captured in MRI images taken from 3 male and 3 female chimps and 6 male and 6 female humans. Mean shape and intensity atlases are computed for each dataset. These atlases are connected diffeomorphically. We then study the volumetric shape differences implied by the correspondence. The significant structural differences and the map itself may be used to assess hypotheses regarding evolutionary changes between these species, as well as provide putative models for further investigation of anatomical differences.

Our technical contribution is a novel, fast estimate to the geodesic metric mapping equations (Miller et al., 2002; Beg et al., 2005). The method computes second-order optimal-in-time geodesic diffeomorphic transformations in the original volumetric domain of the images. Our algorithm for computing the *push-forward* transformation (in addition to the *pull-back*) has two advantages. First, combined with the traditional *pull-back*, it grants facile movement between the Eulerian and Lagrangian reference frames. Computation in the Lagrangian frame is more numerically stable than the Eulerian frame (Donea et al., 2004) thereby allowing larger time steps to be used. Second, we gain numerical efficiency and locally optimal-in-time estimates via the modified midpoint rule, yielding a robust parameterization of the geodesic path. The Lagrangian frame is also more natural for landmark registration. Finally, our metric matching algorithm employs both landmarks and image similarity in the optimization scheme. We apply this image registration tool to the problem of connecting anatomical templates, to our knowledge an unstudied aspect of Grenander's computational anatomy (Grenander, 1993).

2. Image registration methodology

This section briefly reviews deformable image registration methods based on continuum models and details the diffeomorphic model used in our study. Computational anatomy group theory (Grenander and Miller, 1998) is our particular focus.

The group theory tells one how to move between group elements and gives group specific geodesic paths and metrics between those elements. When used in the context of image registration, the theory allows one to compute distances between anatomies, to compose deformable solutions in series and to find large deformation mappings without introducing tears or overlaps. These qualities are essential for solving the problem of finding connections between distinct, but mappable populations, such as that of the human and primate. The benefits of the group theory in computational anatomy and, in particular, for connecting anatomies are highlighted here:

- The invertibility of diffeomorphisms is needed to establish natural transformations from image I to J and from J to I.
- Composability allows us to combine multiple transformations in series. We use this property of diffeomorphisms to connect anatomies.
- Distances (or metrics) that are symmetric and satisfy the triangle inequality are needed for making unbiased measurements of the deformation between anatomies. This is essential for finding "average" anatomy and for quantifying growth and development.

All of these qualities are important for the study in this paper. First, however, we must develop an efficient algorithm to guarantee that we have invertibility, the ability to compose and robust distance measurements. We develop an efficient algorithm for estimating diffeomorphisms and their distances below.

2.1. Overview of algorithmic contribution

We develop a Lagrangian Push-Forward (LPF) method for finding diffeomorphic geodesics. Our technique contrasts with greedy time-independent methods given by Christensen et al. (1996) and Bro-Nielsen and Gramkow (1996) for images and Joshi and Miller (2000) for landmarks. Christensen solves the image matching problem in the Eulerian domain, while Joshi solves in the Lagrangian domain. Neither algorithm explicitly takes the time dimension into account, nor do they generate the inverse transformation directly. We solve both landmark and image problems, either independently or as a balanced variational optimization, in the fixed Lagrangian reference frame. The inverse transformation is derived from the solution in the Lagrangian frame. We gain smoothness in time through a stable numerical method estimating the velocity over a small time increment. These tools combine to give a robust and still efficient estimate of geodesic distance. Furthermore, our method enables direct movement between the static and moving reference frames, allowing both Lagrangian quantities (such as the Jacobian) and Eulerian quantities (such as the arc length of the geodesic) to be easily measured. The notation in the paper is summarized in Table 1.

Table 1
Notation in the body of the paper

Ω :	Domain in $\mathbb{R}^d$
I :	Fixed image
J :	Moving image
$\mathbf{x}$:	Coordinates of material points in the Lagrangian domain
$\mathbf{y}$:	Coordinates in the spatial or Eulerian domain
t :	Time or simulation time
ϕ :	*Pull-back* coordinate map
ϕ^{-1} :	*Push-forward* coordinate map
$(\mathbf{p}_i^I, \mathbf{q}_i^J)$:	Matching landmarks in I and J, respectively

2.2. Background

2.2.1. Static reference frame

High-dimensional image registration with continuum mechanical regularization (Bajcsy and Broit, 1982; Gee et al., 1993; Miller et al., 1993; Christensen et al., 1996) maps anatomy into a common atlas space through a physical deformation model. The goal is to locate a transformation that provides correspondence between the images under consideration, a fixed image, I, and a moving image, J. The variational optimization problem as formulated by Gee (1999), following Bajcsy's pioneering work (Bajcsy and Broit, 1982), finds the solution $\mathbf{u}^*$ as,

$$\mathbf{u}^*(\mathbf{x}) = \operatorname{argmin}_{\mathbf{u}} \left\{ \Pi_R(\mathbf{u}) + \int_\Omega \|I(\mathbf{x}) - J \circ \phi(\mathbf{x})\|^2 \mathrm{d}\Omega \right\}. \tag{1}$$

The Π_R term regularizes $\mathbf{u}(\mathbf{x})$ explicitly. Here, $\phi(\mathbf{x}) = \mathbf{y}$ and the deformation, $\mathbf{u}(\mathbf{x}) = \mathbf{y} - \mathbf{x}$, is measured with respect to the original configuration. This elastostatic formulation warps the moving image into the reference frame provided by I by computing the transformation from I to J. The map ϕ: $I \to J$ gives the *pull-back* of J to the space of I, $\tilde{J} = J(\mathbf{x} + \mathbf{u}(\mathbf{x})) = J \circ \phi(\mathbf{x})$. This change of coordinates is not guaranteed to have an inverse. Many points may map to one point or large or small scale folding may occur.

2.2.2. Grenander's computational anatomy

Computational anatomy uses flows to reposition anatomy as a function of time, $J(\phi(\mathbf{x},t))$, through a map ϕ. The map is an invertible *diffeomorphic transformation* defined on Ω, ϕ:$\Omega \times t \in [0,1] \to \Omega$. Note that the transformation is fixed to be the identity along the border of Ω, such that $\phi(\mathrm{d}\Omega,t) = \mathrm{d}\Omega$. This change of variables smoothly repositions J within space. At convergence, (time $t = 1$), $I(\mathbf{x}) = J \circ \phi(\mathbf{x},1)$ and $J(\mathbf{y}) = I \circ \Psi(\mathbf{y},1)$ with $\phi(\mathbf{x},t) = \Psi(\mathbf{y},s)$ for all $t = 1 - s$. Diffeomorphisms also require $\phi^{-1} \circ \phi = \mathbf{Id}$. The maps may match landmarks as well as images. A landmark is defined as a pair $(\mathbf{p}_i^I, \mathbf{q}_i^J)$ of a priori corresponding subdomains on Ω where the superscript reflects the anatomy to which the landmark is associated.

The variational matching problem is given here with both image and landmark similarities,

$$\inf_{\mathbf{v}} \int_0^1 \left\{ \|\mathbf{v}\|_L^2 + \int_\Omega |I(\mathbf{x}) - J \circ \phi(\mathbf{x})|^2 \mathrm{d}\Omega + \sum_i \frac{1}{\sigma_i} (\phi(\mathbf{q})_i^J - \mathbf{p}_i^I)^2 \right\} \mathrm{d}t. \tag{2}$$

The first term gives the deformation energy, where the choice of functional norm $\|\cdot\|_L$ specifies one's solution

space and will be discussed below. The velocity, $\mathbf{v}$, gives the speed and trajectory of particles moving through a spatial or Eulerian reference frame. The σ_i is variance for the landmarks. The landmark matching approaches exactness as $\sigma \to 0$. Both Eulerian and Lagrangian reference frames will be important for our diffeomorphic image registration algorithm.

This study uses the large deformation metric mapping framework to solve problems of the type in Eq. (2). The theory for these methods was developed largely by Grenander and Miller (1998), Miller et al. (2002) and is connected to work in fluid dynamics (Marsden and Ratiu, 1999; Holm et al., 2004; Hirani et al., 2001) and *o.d.e.*s (Arnold and Khesin, 1992. Grenander defines the anatomical orbit (or shape space) of the atlas or reference anatomy, I, as the set of transformations that map I diffeomorphically to all possible anatomies, $\{J_i\}$. For each J_i, we have $I \circ \phi_i^{-1} = J_i$ and an associated metric telling us how far J is from I. The set of transformations, $\{\phi_i\}$, is chosen to be a mathematical group. Conveniently, there is a group theory associated with viscous fluid flow, the infinite-dimensional group of diffeomorphisms, $\mathscr{G}$.

The diffeomorphism group is defined formally by

$$\mathscr{G} = \{\phi : \Omega \to \Omega | \forall \Psi \in \mathscr{G} : \Psi \text{ and } \Psi^{-1} \text{ differentiable}\}. \tag{3}$$

An additional constraint is that elements of $\mathscr{G}$ must depend smoothly on both arguments, $\mathbf{x}$ and t (Arnold, 1991). Locally, these transformations are affine. Now denote diffeomorphic mappings ϕ and Ψ, such that $\phi(\mathbf{x},t) = \phi(t)$, $\Psi(\mathbf{y},s) = \Psi(s)$, $\phi(0) = \mathbf{x}$ and $\Psi(0) = \mathbf{y}$ with $s = 1-t$. Group elements such as these are generated by the *o.d.e.*,

$$\frac{\mathrm{d}}{\mathrm{d}t}\phi(t) = \mathbf{v}(\phi(t)), \tag{4}$$

where ϕ is in the Lagrangian frame and $\mathbf{v}$ is in the Eulerian frame. Here, the Eulerian velocity with which a particle leaves position $\mathbf{y}$ is given by $\mathbf{v}(\phi(t))$. The velocity in Lagrangian coordinates satisfies $\mathbf{V}(\mathbf{x},t) = \mathbf{v}(\mathbf{y},t)$ (Marsden and Ratiu, 1999).

The $\mathbf{v}$ must satisfy continuity conditions in order to guarantee the existence of these solutions. See, for example, the development for image matching in (Dupuis et al., 1998; Trouve, 1998) or that for fluid mechanics in (Marsden and Ratiu, 1999). The $\mathbf{v}$ must be smooth in the space of definition and the associated norm must be bounded (Miller, 2004). Here, we will use the Sobolev space $\mathscr{V}$ as in (Dupuis et al., 1998). A linear, differential operator both defines the specific group of diffeomorphisms (along with boundary conditions) and insures the smoothness required for integrability and to regularize the solution (Tikhonov and Arsenin, 1977; Dupuis et al., 1998; Marsden and Ratiu, 1999). A common linear operator for computational anatomy, used here, is the modified Laplacian operator,

$$L = \mu\nabla^2 + \lambda\mathbf{Id}, \tag{5}$$

where μ and λ are constants. Integrating the local norm $|L\mathbf{v}|$ over the domain Ω gives the functional norm $\|L\mathbf{v}\| = \|\mathbf{v}\|_L$ with $\|\cdot\|$ the usual L_2 definition.

The final map, $\phi(1)$, is found by integrating the velocities from time zero to time $t = 1$,

$$\phi(1) = \int_{t=0}^{t=1} \mathbf{v} \circ \phi(t)\mathrm{d}t. \tag{6}$$

The metric defined on $\mathscr{G}$ is given by the sum of incremental functional norms in time, thus providing the cost of registration, as well as a metric (Hirani et al., 2001). The length of this diffeomorphic flow is a direct analogy to curve length. The distance between a pair of domains connected via a diffeomorphic flow is a shortest path defined (Grenander and Miller, 1998; Hirani et al., 2001),

$$D(\phi(1)) = \inf_{\mathbf{v}} \int_0^1 \|\mathbf{v}(\phi(t))\|\mathrm{d}t. \tag{7}$$

Minor variations on this definition give the distance between diffeomorphisms ($\phi(0) = g$, $\phi(1) = h$ with $g, h \in \mathscr{G}$) or images ($I \circ \phi^{-1}(0) = I$ and $I \circ \phi^{-1}(1) = J$). This definition provides an appropriate notion of the curved geometric distance between two instances of anatomy.

2.3. Lagrangian push-forward algorithm

We now provide the details of our algorithm which solves both landmark matching and image matching in the Lagrangian domain with a time-optimal technique. That is, the path of each material point (or labeled voxel) is tracked in time, as is the energy of the path. Numerical techniques guarantee robust distance measures and consistent numerical stability. The method uses the push-forward of image I but, at the same time, provides the pull-back of image J to I through both ϕ and ϕ^{-1}. An overview is in Table 2.

2.3.1. Momentum and velocity

The velocity, in general, is found by computing the momentum of the physical system and then finding the Green's kernel for L. The momentum requires computing the variation of the integral in problem (2). Our method uses the push-forward of images and landmarks to, effectively, set ϕ to identity at each moment. We state, without proof, that the momentum minimizing (2) must satisfy at each time (a static view),

$$(L\mathbf{v})_{IJ}(\mathbf{y}) = |I(\mathbf{y}) - J(\mathbf{y})|\nabla(I(\mathbf{y})), \tag{8}$$

for images warped by push-forward, $I \circ \phi^{-1} \circ \mathbf{x} = I \circ \mathbf{y}$, and

Table 2
Overview of the Lagrangian push-forward algorithm

(1)	Find the push-forward, $I \circ \phi^{-1}$ to define the domain, $\mathbf{y}$, on which $\mathbf{v}$ is defined. Use the push-forward method
(2)	Compute $\mathbf{v}$ in Eulerian coordinates. Use the modified midpoint method. This step automatically adjusts the gradient estimate and step-size such that $\frac{dD}{dt} =$ constant, that is, the increment in the distance does not change. This implies the energy of the velocity field is constant in time
(3)	Find $\mathbf{V}$ in Lagrangian coordinates, $\mathbf{V} = \mathbf{v} \circ \phi$, using (e.g. linear) interpolation
(4)	Update ϕ by $\mathbf{V}$. Use the ϕ update method in Eq. (11). Also update the geodesic distance by trapezoidal rule

$$(L\mathbf{v})_{\mathbf{pq}}(\mathbf{p}') = \frac{1}{\sigma_i}(\mathbf{q} - \mathbf{p}'), \tag{9}$$

for the landmarks, where $\phi^{-1}(\mathbf{p}) = \mathbf{p}'$. Both of these equations assume the variation is taken at a static moment and that the image or landmark is pushed forward. The momentum at each iteration is

$$\mathbf{v}(\mathbf{y}) = \frac{w_1(\mathbf{y})}{\gamma_1} K(L\mathbf{v}_{IJ}) + \frac{w_2(\mathbf{y})}{\gamma_2} K(L\mathbf{v}_{\mathbf{pq}}), \tag{10}$$

where K is the Green's kernel for L, the w_i sum to one and the γ_i scale the velocities to have the same L_∞ norm. A pure landmark matching example is in Fig. 1. The Jacobian term that comes from the change of coordinates (Beg et al., 2005) is absorbed in the push-forward of I. The equation (10) is the input to the estimate used in each step of the Modified Midpoint Method (MMM) described in Table 3. Increasing the weighting on the landmarks and allowing the registration to run for long durations approximates exact matching to within subpixel accuracy. An example of a landmarked and non-landmarked image result is in Fig. 2. Combining both landmark and intensity forces during the optimization allows one to balance their relative influence on the solution. Both contribute to the velocity according to their respective weights, which vary across the domain. Image forces are used where landmark forces are absent, similar to the approach used for prior-based curve matching in (Avants and Gee, 2003).

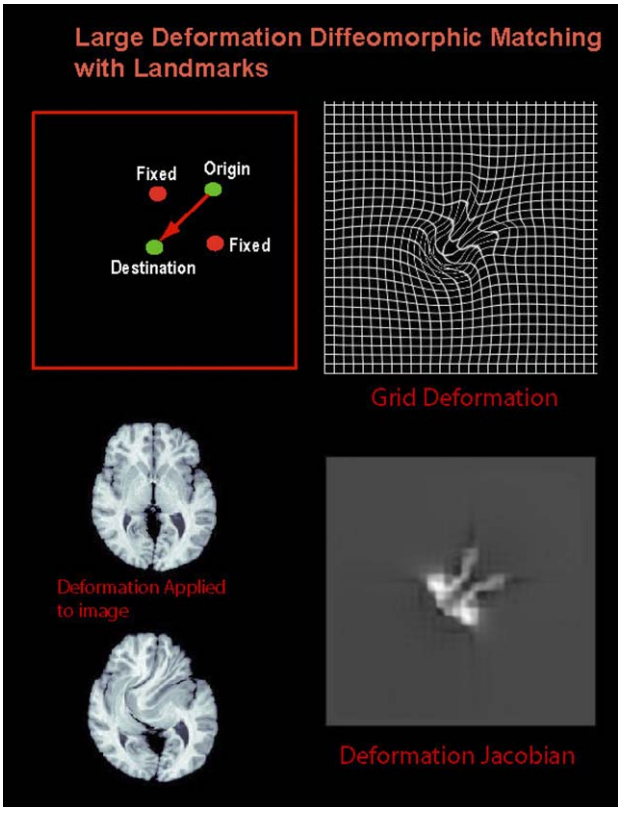

Fig. 1. Langrangian push-forward diffeomorphic landmark matching is illustrated with an example in which one landmark is forced to pass between two others. This type of transformation would typically induce folding. The grid illustrates the smoothness of the transformation.

Table 3
Modified Midpoint Method for $\mathbf{v}$ (MMM)

(1)	Set the initial estimate $z_0 = \mathbf{Id}$
(2)	$z_1 = z_0 + h\mathbf{v}(t, \mathbf{y} + z_0)$
(3)	$z_2 = z_0 + H\mathbf{v}(t + h, \mathbf{y} + z_1)$
(4)	Set the optimal estimate $\mathbf{v}^* = 0.5(z_2 + z_1 + h\mathbf{v}(t + H, \mathbf{y} + z_2))$

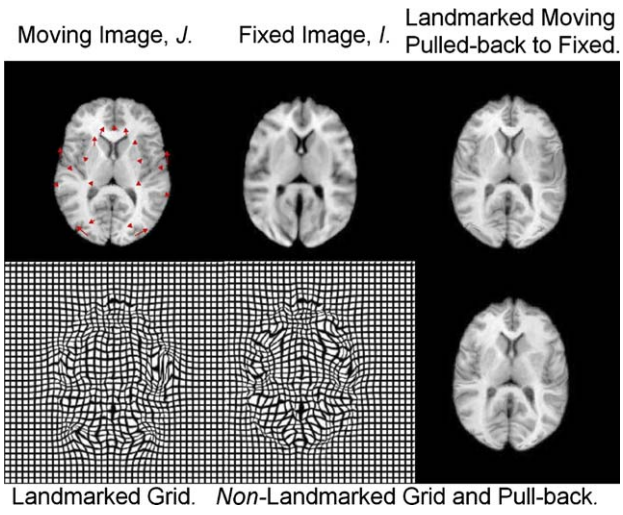

Fig. 2. A two-dimensional, test example showing diffeomorphic registration of human to chimp anatomy, with and without landmarks. The anatomy must be landmarked to guarantee a successful result. Linear landmark trajectories are overlaid on the upper left image. Combining both landmark and intensity forces during the optimization allows one to balance their relative influence on the solution.

2.3.2. Integrating ϕ

The ordinary differential equation generating diffeomorphisms is solved in the Lagrangian frame of reference. The advantages and disadvantages of this reference frame, as compared to the Eulerian frame, are surveyed in (Donea et al., 2004). Our method is, in fact, a combined approach, where Eulerian quantities are computed in the Eulerian domain, but the total solution is stored and monitored in the Lagrangian domain. The LPA algorithm for integrating the transformation ϕ is in Table 2.

Solving for ϕ in the Lagrangian frame is attractive because it allows larger time-steps than does the solution in the Eulerian domain, such as (Christensen et al., 1997; Grenander and Miller, 1998). The geodesic, ϕ, and its length is given by integrating the *o.d.e.* in step 4 of Table 2. The Eulerian velocity estimate comes from the second-order accurate modified midpoint method (Press et al., 2002). The discretization in time is

$$\begin{aligned}
&\frac{\mathrm{d}\phi(\mathbf{x},t)}{\mathrm{d}t} = \mathbf{v}\circ\phi(\mathbf{x},t),\\
&\frac{\phi_{i+1}(\mathbf{x})-\phi_i(\mathbf{x})}{\Delta t} \approx \mathbf{v}\circ\phi_t(\mathbf{x}),\\
&\phi_{i+1} = \phi_i + \Delta t\mathbf{v}\circ\phi_t(\mathbf{x}),\\
&\phi_{i+1} = (\mathbf{Id}+\Delta t\mathbf{v})\circ\phi_i,\\
&\phi_{i+1}(\mathbf{x}) = \mathbf{x}+\mathbf{u}(\mathbf{x})+\Delta t\mathbf{V}(\mathbf{x}) \text{ where } \mathbf{V}(\mathbf{x}) = \mathbf{v}\circ\phi_i.
\end{aligned} \tag{11}$$

The material derivative, in Lagrangian calculations, is just the time derivative (Donea et al., 2004). Thus, $\mathrm{d}\phi/\mathrm{d}t$ is approximated with a simple finite difference. We also adjust Δt such that the Courant–Friedrichs–Levy (CFL) condition is met, that is, arc length of the geodesic is small (spatially) and constant (or the momentum, if known, is conserved (Miller et al., 2003)). An example of image matching with and without the diffeomorphic constraint is in Fig. 3. The algorithm for estimating the Lagrangian velocity is illustrated in Fig. 4.

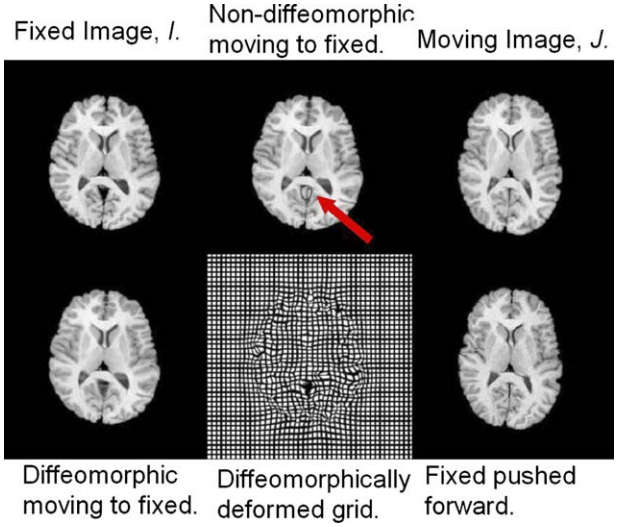

Fig. 3. Langrangian push-forward diffeomorphic image matching is illustrated here. For comparison, a method that uses addition, not composition, is at top center. The topology is violated (at the arrow) when one uses addition of the velocity fields, rather than composition. This is a 2D experiment.

2.3.3. Estimating $\mathbf{v}$

The goal of this method is to find a numerically stable $\mathbf{v}$ estimate and to allow one to guarantee that Eulerian quantities are robustly computed and, if need be, conserved. This is an improvement over the greedy method used in (Christensen et al., 1997). The optimal velocity,

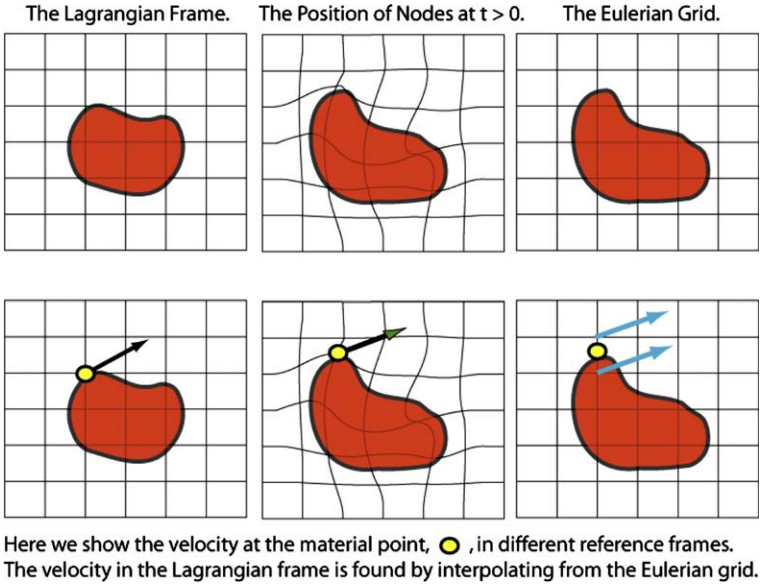

Fig. 4. The use of computational grids for finding the velocity in the Lagrangian reference frame. Interpolating the velocity between the two regular grids guarantees $\mathbf{V}(\mathbf{x},t) = \mathbf{v}(\mathbf{y},t)$.

$\mathbf{v}^*$, is found with the modified midpoint method as described in (Press et al., 2002).

The estimates to the velocity at each iteration are accumulated by MMM with temporal/spatial discretization step $h = H/2$ and H equal to $\bar{h}$, where $\bar{h}$ is the arc length. Constant arc length integration of the velocity norm gives an optimal in time two point trapezoidal estimate to the geodesic distance of equation (7). Constant spacing is required for the trapezoidal rule (Press et al., 2002). The case for step-size $h = H/n$ with $n = 2$ is described in Table 3.

MMM is second-order accurate and requires $n + 1$ evaluations of the $\mathbf{v}$ per iteration. Use of this method improves the estimate of the geodesic distance, the momentum and improves the convergence time over simpler methods such as the trapezoidal rule or explicit Euler integration. It is also more efficient than second-order Runge–Kutta. We use MMM to average the velocity over a small time increment but trapezoidal rule to integrate the distances and the flow in time (Avants and Gee, 2004b). A comparison of this method to Eulerian (Christensen et al., 1996) image registration is shown in Table 4. The LPF method shows similar time performance with improved solution smoothness and distance measurements, without the MMM method. The MMM method is more costly in time performance but improves the estimate to the geodesic distance. Comparison with Christensen's Eulerian method is in Table 4.

2.3.4. Image push-forward

Pushing the coordinate map forward from the Lagrangian domain allows us to compute the velocity in the Eulerian frame. The warped domain, $\mathbf{x} \rightarrow \mathbf{y}$, is mapped to a new regular grid on which we compute $\mathbf{v}$ and $L\mathbf{v}$ as in Fig. 4. Warping the reference domain $\mathbf{x}$ to the position $\mathbf{y}$ given by $\phi^{-1}(\mathbf{x})$ permits regularization in the Eulerian domain but to continue to solve in the Lagrangian domain via ϕ. The push-forward constitutes an inverse problem within the algorithm. It is found by integrating the negative velocity fields in the Lagrangian frame forward in time. The numerical integration of $\mathrm{d}\phi^{-1}/\mathrm{d}t$ is similar to that described in Eq. (11) and is shown in Table 5. This generates ϕ^{-1} in the Eulerian frame.

For generality, Table 5 illustrates the push-forward method from an identity initialization. The algorithm's implementation, however, stores the last estimate to ϕ^{-1} which is used as the initialization each time the method is called, therefore allowing it to converge within a few (typically one) iterations. This algorithm is effective within our registration method and as a general procedure for the inversion of diffeomorphic maps. The existence of a solution is guaranteed by the integrability condition established for diffeomorphic image registration (Dupuis et al., 1998), while uniqueness comes from the uniqueness theorem of *o.d.e.*s (Arnold, 1991).

Table 4
Comparison of distances between human cortical images generated by a greedy Eulerian (EUL) algorithm, the Lagrangian (LPF) algorithm without the MMM and the Lagrangian algorithm with the MMM (MMM)

Case	EUL Intensity Dist	EUL Dist	CPU time	Deformation
1	1.65	2.39	1	0.40
2	1.64	2.56	1	0.40
3	1.73	2.61	1	0.42
4	1.63	2.52	1	0.39
5	1.67	2.52	1	0.42
	MMM Intensity Dist	MMM Dist	CPU time	Deformation
1	1.65	1.85	1.41	0.38
2	1.63	1.73	1.54	0.38
3	1.73	2.15	1.60	0.43
4	1.62	1.82	1.63	0.38
5	1.65	1.86	1.63	0.42
	LPF Intensity Dist	LPF Dist	CPU time	Deformation
1	1.66	2.18	0.88	0.38
2	1.65	2.23	0.93	0.38
3	1.75	2.40	0.96	0.41
4	1.64	2.23	0.98	0.39
5	1.68	2.18	0.98	0.41

Distances given by MMM are shorter than both the LPF and EUL method and the intensity differences are smaller. The LPF algorithm is comparable in speed to the EUL algorithm. The EUL implementation is our own, based on (Christensen et al., 1996). CPU time is given as a ratio with the EUL execution time. The deformation column indicates the value of the map's elastic deformation energy. It is significant that the Eulerian method has the most deformation. This is attributed to the EUL method's relative lack of stability and its use of the material derivative in the velocity integration. A set number of iterations and a constant time step of 0.2 pixels was used in this comparison.

Table 5
Push-Forward Method

(1)	Output $\phi^{-1}(\mathbf{y}) = \mathbf{x}$, given $\phi(\mathbf{x}) = \mathbf{y}$. Denote r as the image resolution
(2)	Set $\phi^{-1} = \mathbf{Id}$. Denote $\tilde{\mathbf{y}}$ as the current estimate to the Eulerian domain defined by $\phi(\mathbf{x})$. At time zero, $\tilde{\mathbf{y}} = \mathbf{x}$. At convergence, $\tilde{\mathbf{y}} = \mathbf{y}$
(3)	**While** $(\|\mathbf{y}(\tilde{\mathbf{y}}) - \tilde{\mathbf{y}}\|_\infty > 0.5r)$
(4)	Compute $\mathbf{v}^{-1}(\mathbf{x}) = \phi(\mathbf{x}) - \tilde{\mathbf{y}}(\mathbf{x})$
(5)	Integrate ϕ^{-1} such that $\phi^{-1}(\tilde{\mathbf{y}}, t+1) = \phi^{-1}(\tilde{\mathbf{y}}, t) + \gamma \mathbf{V}^{-1}(\tilde{\mathbf{y}})$, where $\mathbf{v}^{-1}(\mathbf{x})$ is warped to the Eulerian domain. The local scalar parameter, γ, sets the maximum L_∞ norm of $\mathbf{v}^{-1}$ to be half of the image discretization size, r
(6)	**end While**

3. Experimental design

The methods described above guarantee invertible diffeomorphic transformations, the ability to compose transformations and also robust distance estimates. The diffeomorphisms may also be generated by both landmark and image similarity. We will now use this algorithm for morphometry of the chimpanzee and human cortex.

3.1. Inter-atlas comparison

An open question in computational anatomy is how to connect disjoint anatomical templates, such as the primate and *Homo sapiens* cortex. The shape space for each species is generated from a different atlas or reference, that is, one cannot generate a human anatomical instance, I^{H}, from a chimp anatomy, I^{C}. Selecting any single species atlas is bound to bias the study and introduce error caused by varying tissue characteristics, acquisition resolution as well as intrinsic difference in the anatomy. For example, gray matter and white matter intensities are (in MRI) less distinct in the chimpanzee, as shown in the histograms of Fig. 5.

Large deformation atlases may be used to compactly represent a group and its shape and/or intensity variations. Large deformation atlas construction methodology (Thompson et al., 1999; Avants and Gee, 2004b; Joshi et al., 2004) combined with diffeomorphic inverse consistent methods (Avants and Gee, 2004a) may aid in constructing inter-species atlases, although significant problems arise. No optimal inter-species atlas can be constructed without positing a "missing link" anatomy. These averaging models do not permit one to average shape and intensity between two populations that do not exist in the same shape space and that have close, but different tissue characteristics. That is, only tissues with similar intensity characteristics can be averaged linearly and only shapes that come from the same anatomical shape space may be averaged by our current non-linear shape averaging models.

Therefore, we base our study on a connection between the anatomical shape spaces, through the most representative atlases. We approximate transformations that bring the evolutionarily distinct atlases as close as possible in a minimum-effort sense. A simple, shape-only illustration is shown in Fig. 6. This approach gives a least action comparison between the shape spaces with the constraint that the populations connect only through least biased (having fewest individual characteristics) mean representations. The advantage, here, is that the intra-species shape variance is gained from comparison to the optimal single-species atlas. The inter-species maps may be gained from multiple putative models (as in Essen (2004b)) or from expert landmarking.

Note an important property of this model. Assume the correspondences are correct in the inter-species map and, separately, in the intra-species maps. Composing these transformations will bring the full datasets into anatomical–functional correspondence. This property gives *maximal* benefit from *minimal* a priori knowledge (expert intervention).

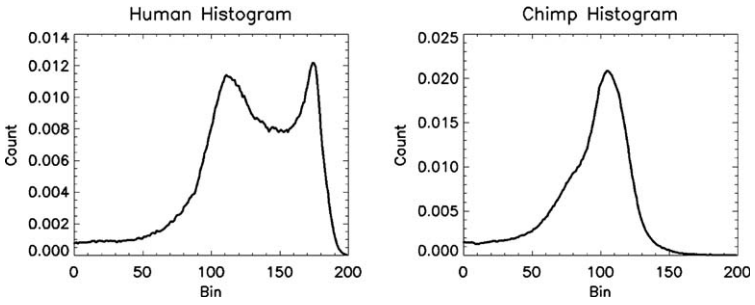

Fig. 5. The tissue histogram for the human (left) and the chimpanzee cortex (right). The gray and white matter classes are mixed in the chimpanzee, but are distinct in the human.

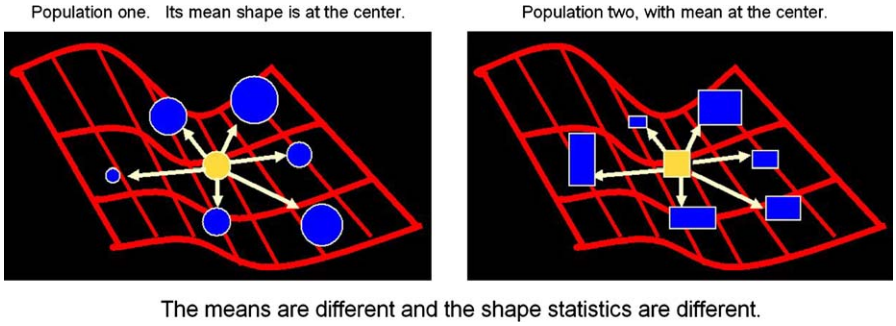

Fig. 6. This figure uses two simple shape spaces to illustrate the idea of mapping between atlas shapes. The only variable, here, is the shape and shape transformations, not the intensity.

This method for connecting anatomical templates, gives the relationship of the human atlas group, $\{I_{\mathrm{H}} \circ \phi_i^{-1}\}$, to the group for the chimp atlas, $\{I_{\mathrm{C}} \circ \phi_j^{-1}\}$, through a single inter-species map, Ψ^{HC}, and its effect on the first order statistical moment. The resulting inter-species transformation moves between representative anatomies (atlases), $\Psi \in \mathcal{G} : \bar{I}^{\mathrm{H}} \rightarrow \bar{I}^{\mathrm{C}}$. Mapping an individual human to the chimpanzee atlas is performed through composition, such that $(J_i^{\mathrm{H}} \circ \phi_i(1)) \circ \Psi^{\mathrm{HC}}(1)$ moves the human anatomy to the chimp space. See Fig. 7. The distances in each shape space are not changed by Ψ or Ψ^{-1} due to the right invariance of the metric (Marsden and Ratiu, 1999) defined on $\mathcal{G}$.

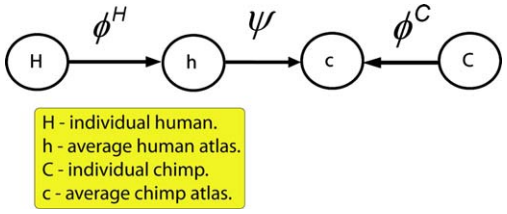

Fig. 7. The connections between individuals and the atlases, through composition. Connections in the directions opposite the arrows are given by the inverse maps, $\phi^{-1\mathrm{C}}$, $\phi^{-1\mathrm{H}}$, Ψ^{-1}.

An illustration of the full morphometry method is in Fig. 8. The inter-species map connects the single-species shape spaces through a functionally and anatomically based geodesic path. That is, Ψ^{HC} *finds the shortest path connecting the means of the shape distributions*, given functional and anatomical constraints. Preferably, an inverse consistent large deformation method should be used (Avants and Gee (2004a)). This allows one to realign the intra-species anatomy, via composition, in a single species space in order to compare the volumetric shape information (Ashburner et al., 1998; Ashburner and Friston, 2000; González Ballester et al., 1999).

Our primary goal for this study is to quantify the functional anatomic differences that exist between chimp and human cortices. For this purpose, we map between chimpanzee and *H. sapiens* cortex through 62 expert

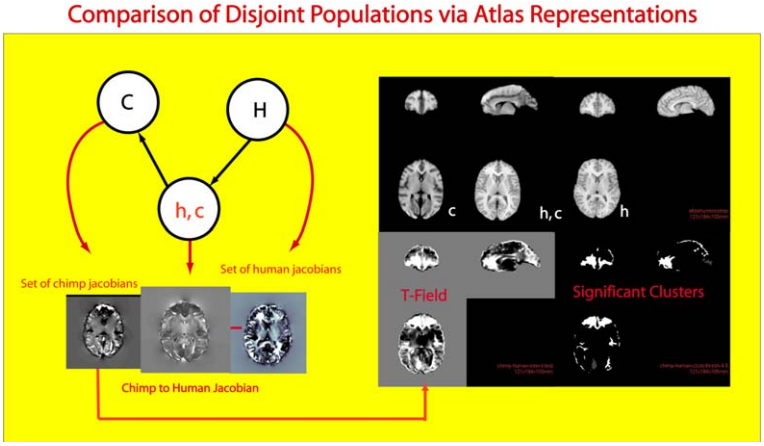

Fig. 8. Composition-based morphometry. Each circle contains a population with an anatomical shape space (a set of transformations). The red arrows emanating from each circle show the Jacobians generated from the shape spaces. Each black arrow indicates a connection between the populations and implies a composition of transformations. The right half of the figure shows example quantities derived from the Jacobian comparison including the T-field and the significant clusters. The data shown in this image are example data, not the final result. See also Fig. 7. (For interpretation of the references to colour in this figure legend, the reader is referred to the web version of this article.)

Table 6
Inter-species right central sulcus functional landmarks (mm^2)

Functional association	Chimp landmark	Human landmark
Pharynx	67 158 113	64 138 108
Tongue	69 158 124	63 142 117
Face	74 154 131	69 133 137
Thumbs	70 145 133	79 133 148
Hand	72 132 141	90 118 159
Arm	81 127 150	100 116 162
Trunk	95 128 158	104 115 166
Leg	106 121 165	114 113 167

annotated landmarks. Some of the 62 points were chosen strictly on the basis of anatomy, rather than function, because of the difficulty in identifying exactly homologous behavioral functions in chimpanzees and humans (e.g., only human cortices process language). However, in three key areas homologous functional information could be used to identify landmarks.

In particular, mapping of the motor cortex by electrical stimulation has been performed on both chimpanzees (von Bonin and WS, 1950) and humans (Penfield and Rasmussen, 1950), reflected in the landmarks described in Table 6. The location of the planum temporale also appears to be functionally and anatomically homologous (Gannon et al., 1998). In addition, it is known that the primary visual cortex (Brodmann's area 17) in chimpanzees extends quite a bit further anteriorly than does the same area in humans (Brodmann, 1909).

In summary, the functional surface landmarks are chosen to:

- functionally reparameterize the central sulcus,
- bring the primary visual cortex and olfactory sulcus into alignment,
- and bring the planum temporale into approximate alignment.

These landmarks are visualized in Fig. 9. After registration, all landmarks are brought into alignment to within their associated variance.

3.2. Statistical morphometry

Voxel-based morphometry is often used to study shape differences in populations via the methods of SPM (Good et al., 2001; Ashburner et al., 1998). The basic unit of measurement in this study is the Jacobian, which measures the local dilatation or contraction of the volume under the action of the map. Jacobians are denoted $\{\mathcal{J}_i^{\mathrm{H}}\}$ for human maps, $\{\mathcal{J}_j^{\mathrm{C}}\}$ for chimpanzee maps and $\{\mathcal{J}_i^{\mathrm{HC}}\}$ for the inter-species Jacobians. They are derived directly from the registration maps. We thus must first find the within-species and then between-species maps.

3.2.1. Within-species variation

The chimps were initially aligned into the human space by similarity transformation. The diffeomorphic inter-species map thus recovers only non-rigid deformation. We computed the maps, $\{\phi_j^{\mathrm{C}}\}$ and $\{\phi_i^{\mathrm{H}}\}$, using the large deformation setting described in Eq. (2) without landmarks. The reference image for each species is the anatomy that locally minimizes the group-wise large deformation distance summed over the whole dataset (7). The shape averaging method described in (Avants and Gee, 2004b) was used to generate the shape atlases and was followed by intensity averaging. The major inter-species features (ventricles, central sulcus, visual cortex, frontal lobes) are well-aligned for each within-species dataset without the need for landmarking. These same features do require landmarking for the inter-species mapping to be correct. The topology preserving nature of the deformation may be seen in Fig. 10. The map between the two most representative (average shape and average intensity) anatomies is in Fig. 11.

3.2.2. Between-species variation

The inter-species log-Jacobians are given by the sum of the ϕ_i^{H} log-Jacobian with the Ψ^{HC} log-Jacobian,

$$\log \mathcal{J}_i^{\mathrm{HC}} = (\log \mathcal{J}_i^{\mathrm{H}}) \circ \Psi^{\mathrm{HC}}(1) + \log \mathcal{J}^{\mathrm{HC}}.$$

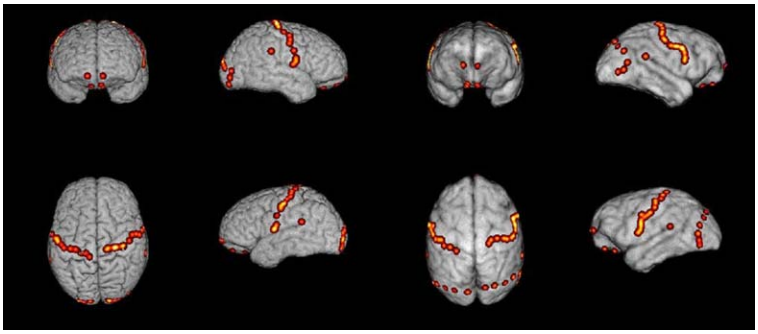

Fig. 9. The surface (functional) landmarks are shown on the surface of the human and chimpanzee shape atlases. The major landmarks are on the plenum temporale, central sulcus and on the boundaries of the visual cortex.

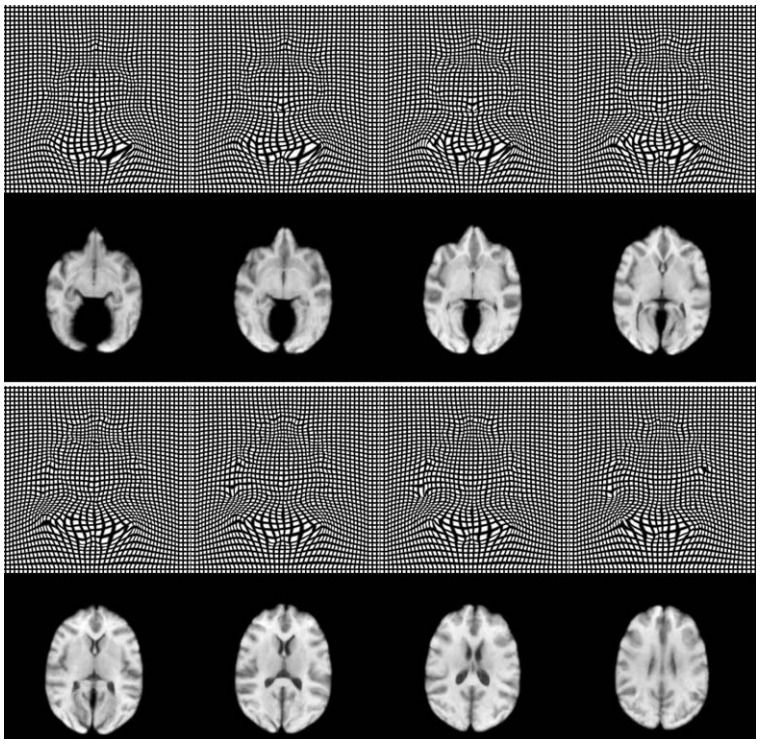

Fig. 10. The grid of the landmark induced deformation from chimp to human. Note that the frontal lobe shrinks and the visual regions enlarge and curve laterally.

Note that, after composition with Ψ^{HC}, the chimp and human to chimp Jacobians, $\mathcal{J}_i^{HC}$, are in the same space. We then statistically compare the datasets $\{\log \mathcal{J}_j^{C}\}$ and $\{\log \mathcal{J}_i^{HC}\}$, where each Jacobian is smoothed by a Gaussian filter with unit variance.

3.2.3. Confidence testing

Permutation testing should be used to gain statistics from composition-based morphometry, as it is a non-parametric model. However, this is a time consuming and expensive route. We will use the standard Student's *t*-statistic giving the probability that two sample populations X and Y have significantly different means. Student's *t*-statistic assumes that data are drawn from populations with the same true variance. This is likely not the case for the chimpanzee and human population. Thus, the *t*-statistic remains a useful qualitative way to view the data that will reveal if the effect of the map Ψ^{HC} on the means is within the variance of each populations' statistics. Results of permutation testing (an empirical technique) with 1000 permutations show similar results, for large structures such as the pre-frontal lobe, to those given by thresholding the uncorrected *t*-statistic at *p*-value 0.001.

3.3. Materials

3.3.1. Image acquisition

The structural data were obtained from two different MRI acquisition sequences. The primate brain scans were obtained from Yerkes Regional Primate Research Center. The scans were T1 weighted, TR = 19.0 ms, TE = 8.5 ms, across subject the slice thickness varied from 1.4 to 2 mm, and in-plane spatial resolution varied from 0.78 to 0.70 mm^2. *H. sapiens* brain scans were obtained from healthy volunteers (approval was obtained from the U.C. San Francisco and University of Pennsylvania IRBs). These scans were T1-weighted, with TR = 32 ms, TE 8 ms, with in-plane resolution of 0.94 mm^2. Female scans had slice thickness of 1.5 mm; male scans had slice thickness of 0.99 mm.

3.3.2. Computers and software

The computations were performed on a PowerMac G5 with 4.5 GB of memory. Preprocessing steps included inhomogeneity correction, extraction of the brain from the head and then semi-automated segmentation of the cerebral cortex using Analyze software. This gave us the required structural data for analysis. The data were all initially aligned to a common image space, defined by arbitrarily selecting one of the human brains. The novel numerical methods were implemented within the Insight Tool Kit (ITK) (Yoo, 2003).

3.4. Interpretation of morphometric study

These experiments do not claim to be a perfect representation of the actual inter-species map. The extent

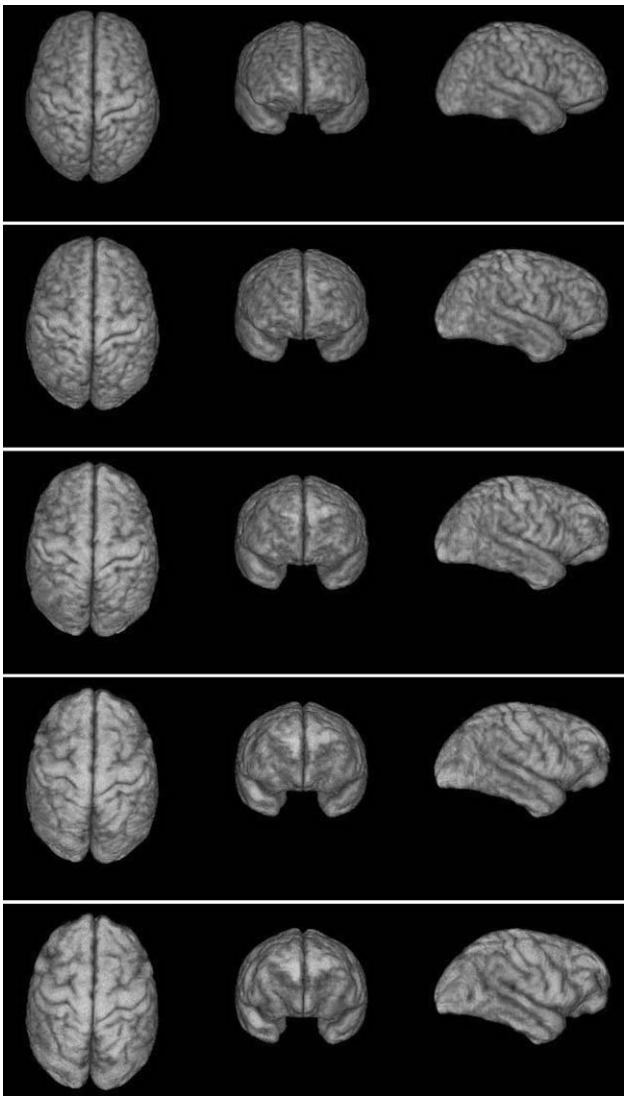

Fig. 11. The mean shape and intensity human (top) is mapped such that it takes on the appearance of the mean shape and intensity chimp cortex (bottom). We note that this last image is in fact the repositioned human anatomy but that it looks nearly identical to the chimp anatomy (at least from the surface view). The functionally based reparameterization of the central sulcus may be seen in the lateral view.

to which they result in a valid representation of the size and location of the differences depends on the extent to which: (1) the landmarks were correctly chosen; (2) the mapping in non-landmarked areas is approximated by the diffeomorphic flow methods used here; (3) the specimens used are representative of their respective species. An additional interesting question is whether a diffeomorphism is a viable model of the inter-species map. Assessing this question is one goal of this study. In fact, we have found that for the chimpanzee and human cortex, the diffeomorphic model appears to be reliable, at least from a structural standpoint. This is supported by the topologically similar functional positions found along the central sulcus, as described in Section 3.1, as well as Van Essen's studies based on surface diffeomorphisms (Essen, 2004a).

The methods aim to produce the least biased geodesic map with the information at hand. Even given the limitations, they provide quite a bit more resolution of the differences between chimp and human than has been assessed using more traditional methods of image analysis, which typically involve hand-delineating (with consequent likely error) specific regions of interest. This method enables a global assessment of differences and allows us to visualize areas of likely evolutionary change without specific a priori focus on regions. This method also summarizes inter-population information in a single time-series of images, as in Fig. 11. An important extension will be to make this inter-population map probabilistic.

One area of particular interest in primate comparisons is the prefrontal lobe, which some studies have suggested is relatively (and absolutely) substantially larger in humans (Blinkov and Glezer, 1968; Brodmann, 1912; Bush and Allman, 2004; Holloway, 1968, 2002), but others conclude that it is as large or only slightly larger relative to brain size as is typically found in primates (Holloway, 1992, 1999). Several studies have concluded that the entire frontal lobe (of which the prefrontal is only a portion) is no larger in humans than one would predict (Rilling and Insel, 1999; Schoenemann and Glotzer, 2003; Semendeferi et al., 1998). The methods used here avoid the need for detailed prior manual delimitation, and allow for

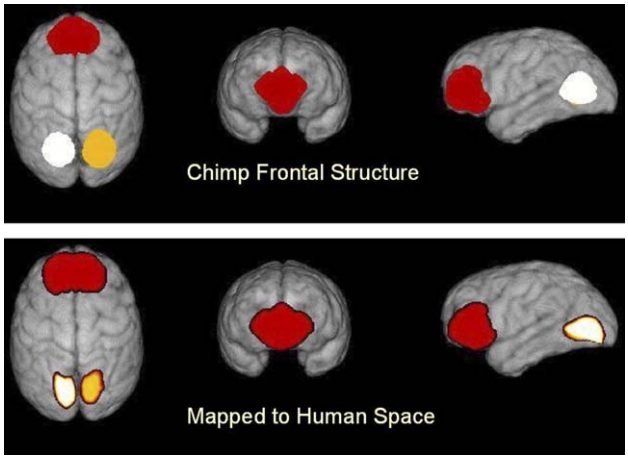

Fig. 12. Semi-automated segmentations mapped between chimp and human. The structures are arbitrarily color-coded such that all connected pixels have the same appearance. These segmentation blobs were placed approximately in the prefrontal region and near the visual cortex in the chimpanzee. The action of the map on the blobs confirms that the chimpanzee tends to have relatively larger visual cortex and smaller prefrontal regions. Because these manual segmentations are defined on the chimp, they had to be pushed forward to the human but are still overlaid on the chimp.

a simultaneous assessment of the relative size of areas across the entire cortex. The average human and average chimp, in our datasets, show a doubling in relative prefrontal size. This is in support of the generally accepted value.

We visualize these regional results by showing the action of ϕ^{-1} on manually segmented structures in Fig. 12 and structures segmented from the Jacobian between average chimp and human in Fig. 13. Statistically segmented structures are rendered in Fig. 14. The structures where the human is relatively larger have p-value <0.001 and t-test greater than zero. The structures where the chimp is relatively larger have p-value <0.001 and t-test less than zero. We analyze, in particular, the size of the automatically segmented prefrontal structure, in Fig. 15 and the Jacobian-derived structure in Fig. 13. Both segmentations of this structure show that it is 2.03 times larger, in relative terms, in the human. Our experiments therefore confirm the generally accepted relative size difference of the pre-frontal lobe in a small set of chimpanzee and human cortices. Furthermore, the statistical segmentation suggests boundaries of the likely areas of increased size, as in Figs. 14 and 15. These studies will ultimately help map the evolution of brains across primates and even mammals. The functional implications of these differences also elucidate the evolution of brain and behavior in our own lineage.

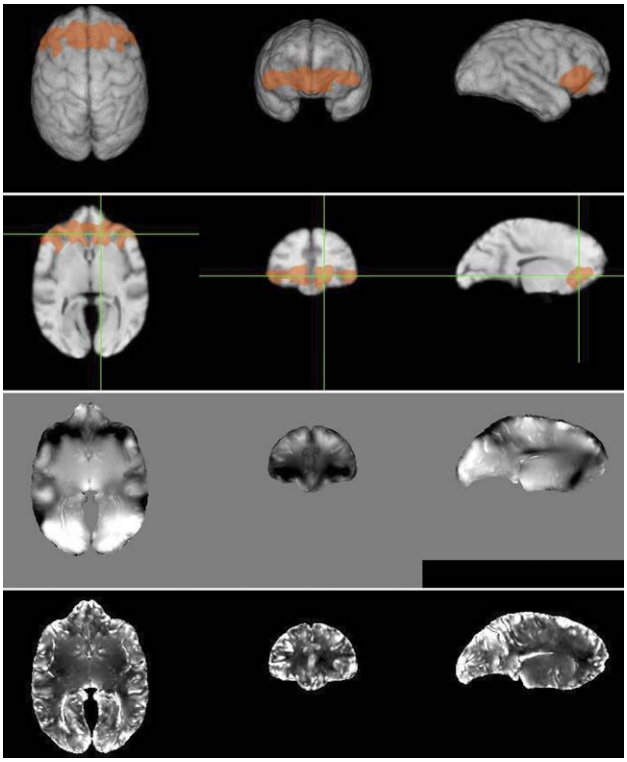

Fig. 13. Semi-automated segmentations of the approximate prefrontal region (top two rows, 2.03 times relatively larger in the human). Dark regions indicate the *H. sapiens* structure is relatively larger, while bright regions indicate the chimp structure is relatively larger. The structure was segmented by placing a level set seed in the general area of the prefrontal region in the Jacobian image and allowing the seed to expand, for fixed time, into the areas of increased relative human size. The average human to chimp log-Jacobian image is in the third row from top. The variance of the human to chimp log-Jacobian image is in the bottom row.

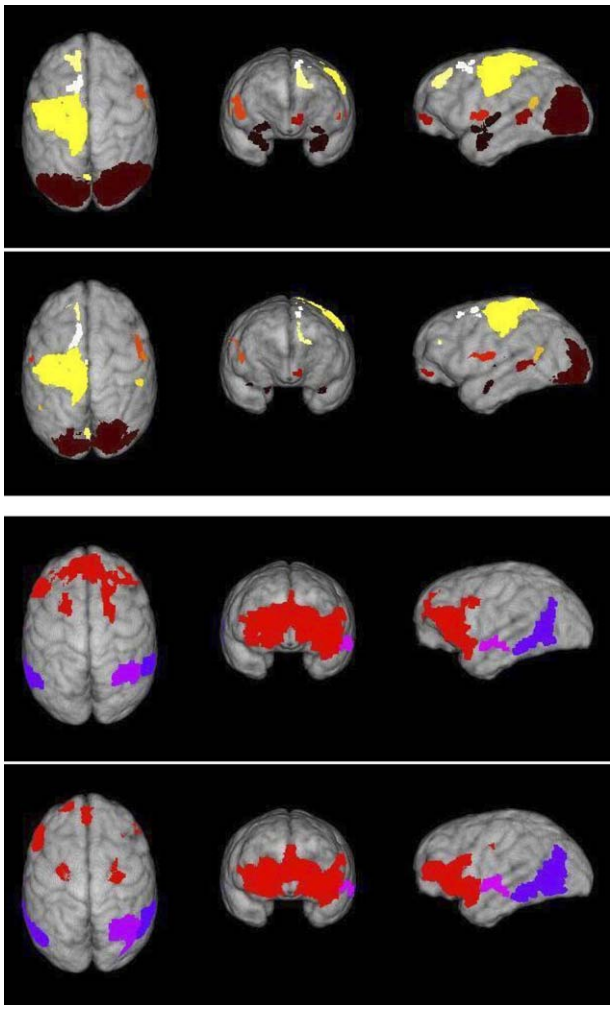

Fig. 14. Structures that appear relatively larger in the chimp (top) pushed forward to the human size (top middle) and human (bottom middle) pushed forward to the human size (bottom). The structures are arbitrarily color-coded such that all connected pixels have the same appearance. Because these statistical segmentations are defined on the chimp, they had to be pushed forward to the human. Of particular interest is the asymmetry of the structures that are relatively significantly larger in the chimp. This is caused by the asymmetry in functional reparameterization of the primary motor cortex, indicating that the left side of the human cortex has undergone greater morphological change than the right. This is consistent with the fact that some key aspects of language processing are lateralized to the left hemisphere in most humans. The regions where human is relatively larger are the prefrontal (as expected) and a few lateral structures that may be associated with language development. We intend to do a more detailed analysis in a separate text. Note that some smaller structures are visible in one view and not the other because of different surface depths.

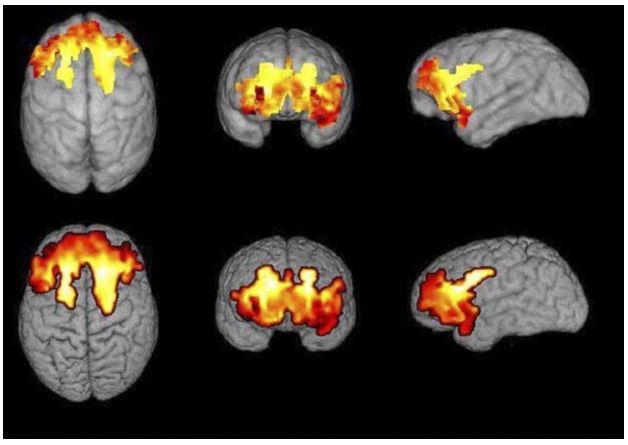

Fig. 15. Prefrontal results. The statistically segmented prefrontal region is in both the chimp (top) and human (bottom). The color indicates the local chimp to human Jacobian value (red lower, yellow higher). The prefrontal region is shown to be statistically relatively larger in humans by the analysis of the map's action on the local volume of structures. The prefrontal volume as defined in the chimp image has a total size increase of 2.03 when it is moved to the human domain. This is almost identical to the prefrontal size difference between chimp and human as computed by other researchers using other methods (Deacon, 1997). Because the statistics are defined on the chimp, the prefrontal segmentation had to be pushed forward to the human. (For interpretation of the references to colour in this figure legend, the reader is referred to the web version of this article.)

4. Conclusion

We presented the LPA algorithm for minimizing Eq. (2) that incorporates an inverse transformation, in-time optimization and a robust velocity estimate. This leads to improved estimates of geodesic distances over greedy, Eulerian gradient descent techniques. The algorithm solves the diffeomorphism *o.d.e.* in the Lagrangian reference frame, but integrates the inverse transformation as well. This sub-algorithm is efficient as shown by comparison to Eulerian methods. Furthermore, longer time steps may be used with Lagrangian techniques. Future work on this algorithm may consist of adding post-processing of the geodesic path (Beg et al., 2005). We also intend to investigate the Euler–Lagrange equations derived by Miller et al. (2002) and deeper connections to work in fluid mechanics (Holm et al., 2004).

The LPA algorithm was used in concert with atlas-building methods to develop a variational motivation for connecting between anatomical templates. These principles lead naturally to composition-based morphometry. The motivation for these techniques was given by the lack of justification for using a single species atlas for an inter-species study. Furthermore, it is untenable to build an inter-species optimal atlas with current techniques in imaging and atlas construction. For these reasons, our inter-species maps were based on detailed landmarking of functional–anatomical homologues found on the most representative, average atlas images. Future work will further develop theory for connecting anatomical shape spaces and for composition-based morphometry.

Our population-based quantitative methods produced values for the estimated size difference between human and chimp prefrontal regions that support common estimates in the literature. We computed the difference in prefrontal size between our average chimp and average human as 2.03. Many other interesting structures of difference between chimp and human were found, but have yet to be analyzed in detail. We are currently investing in a more detailed analysis of regions of difference, especially along the central sulcus, in the visual cortex and in areas of the brain associated with language development. Asymmetry analysis is also fundamental for understanding the difference in the evolution of the chimpanzee and human cortex. We also intend to investigate the effect of different homologue choices on the inter-species map. Finally, we hope to collect more data to aid in expanding the relevance of a full non-parametric statistical study using these methods.

Acknowledgments

The authors thank James Rilling and Thomas Insel for providing the chimpanzee MRI, and Murray Grossman for the human male MRI used in this study. We also thank L. Daniel Glotzer and Michael J. Sheehan for help processing the scans. This work was supported by the USPHS under Grants DA015886, HL71770, LM03504 and NS045839.

References

Arnold, V.I., 1991. Ordinary Differential Equations. Springer Verlag, Berlin.

Arnold, V.I., Khesin, B.A., 1992. Topological methods in hydrodynamics. Ann. Rev. Fluid Mech. 24, 145–166.

Ashburner, J., Friston, K., 2000. Voxel-based morphometry – the methods. Neuroimage 11, 805–821.

Ashburner, J., Hutton, C., Frackowiak, R., Johnsrude, C.P.I., Friston, K., 1998. Identifying global anatomical differences: deformation-based morphometry. Hum. Brain Mapp. 6, 348–357.

Avants, B., Gee, J.C., 2003. Formulation and evaluation of variational curve matching with prior constraints. In: Gee, J.C., Maintz, J.B.A., Vannier, M.W. (Eds.), Biomedical Image Registration. Springer Verlag, Heidelberg, pp. 21–30.

Avants, B., Gee, J., 2004. Symmetric geodesic shape averaging and shape interpolation. In: Computer Vision Approaches to Medical Image Analysis (CVAMIA) and Mathematical Methods in Biomedical Image Analysis (MMBIA) Workshop 2004 in conjunction with the Eighth European Conference on Computer Vision, Prague, CZ, pp. 99–110.

Avants, B., Gee, J., 2004b. Geodesic estimation for large deformation anatomical shape and intensity averaging. Neuroimage (Suppl. 1), S139–S150.

Bajcsy, R., Broit, C., 1982. Matching of deformed images, In: Sixth International Conference on Pattern Recognition, pp. 351–353.

Beg, F., Miller, M., Trouve, A., Younes, L., 2005. Computing large deformation metric mappings via geodesic flows of diffeomorphisms. Int. J. Comp. Vision 61, 139–157.

Blinkov, S.M., Glezer, I.I., 1968. The Human Brain in Figures and Tables. Plenum Press, New York.

Bookstein, F.L., 1992. Morphometric Tools for Landmark Data: Geometry and Biology. Cambridge University Press, New York.

Brodmann, K., 1909. Vergleichende Lokalisationsiehre der Grosshirnrinde in ihren Prinzipien Dargestellt auf Grund des Zellenbaues, Leipzig.

Brodmann, K., 1912. Neue ergebnisse ber die vergleichende histologische localisation der grosshirnrinde mit besonderer bercksichtigung des stirnhirns. Anatomischer Anzeiger supplement 41, 157–216.

Bro-Nielsen, M., Gramkow, C., 1996. Fast fluid registration of medical images. In: Proceedings of the Visualization in Biomedical Computing. Springer Verlag, Hamburg, pp. 267–276.

Bush, E.C., Allman, J.M., 2004. The scaling of frontal cortex in primates and carnivores. Proc. Natl. Acad. Sci. USA 101 (11), 3962–3966, 0027-8424 Journal Article.

Christensen, G.E., Rabbitt, R.D., Miller, M.I., 1996. Deformable templates using large deformation kinematics. IEEE Trans. Image Process. 5 (10), 1435–1447.

Christensen, G.E., Joshi, S.C., Miller, M.I., 1997. Volumetric transformation of brain anatomy. IEEE Trans. Med. Imaging 16 (6), 864–877.

Deacon, T.W., 1997. The Symbolic Species: The Co-evolution of Language and the Brain. Norton, New York.

Donea, J., Huerta, A., Ponthot, J.-P., Rodriguez-Ferran, A., 2004. Encyclopedia of Computational Mechanics. Wiley, New York (Chapter: Arbitrary Lagrangian–Eulerian Methods).

Dupuis, P., Grenander, U., Miller, M.I., 1998. Variational problems on flows of diffeomorphisms for image matching. Quart. Appl. Math. 56 (3), 587–600.

Essen, D.C.V., 2004a. Surface-based approaches to spatial localization and registration in primate cerebral cortex. Neuroimage (Suppl. 1), S97–S107.

Essen, D.C.V., 2004b. The Visual Neurosciences. MIT Press, Cambridge, MA, pp. 507–521, (Chapter: Organization of visual areas in macaque and human cerebral cortex).

Essen, D.C.V., Drury, H.A., Joshi, S., Miller, M.I., 1998. Functional and structural mapping of human cerebral cortex: solutions are in the surfaces. Proc. Natl. Acad. Sci. USA 95, 788–795.

Essen, D.C.V., Lewis, J.W., Drury, H.A., Hadjikhani, N., Tootell, R.B.H., Bakircioglu, M., Miller, M.I., 2001. Mapping visual cortex in monkeys and humans using surface-based atlases. Vis. Res. 41, 1359–1378.

Gannon, P.J., Holloway, R.L., Broadfield, D.C., Braun, A.R., 1998. Asymmetry of chimpanzee planum temporale: humanlike pattern of wernicke's brain language area homolog. Science 279, 220–222.

Gee, J.C., 1999. On matching brain volumes. Pattern Recogn. 32, 99–111.

Gee, J.C., Reivich, M., Bajcsy, R., 1993. Elastically deforming a 3D atlas to match anatomical brain images. J. Comput. Assist. Tomogr. 17, 225–236.

González Ballester, M.A., 1999. Morphometric analysis of brain structures in MRI. Ph.D. thesis, University of Oxford.

Good, C.D., Johnsrude, I.S., Ashburner, J., Henson, R.N.A., Friston, K.J., Frackowiak, R.S.J., 2001. A voxel-based morphometric study of ageing in 465 normal adult human brains. NeuroImage 14, 21–36.

Grenander, U., 1993. General Pattern Theory. Oxford University Press, New York.

Grenander, U., Miller, M.I., 1998. Computational anatomy: an emerging discipline. Quart. Appl. Math. 56 (4), 617–694.

Han, X., Xu, C., Prince, J., 2003. A topology preserving level set method for geometric deformable models. IEEE Trans. Pattern Anal. Machine Intelligence 25 (6), 755–768.

Hirani, A.N., Marsden, J.E., Arvo, J., 2001. Averaged template matching equations. In: Proceedings of Energy Minimization Methods in Computer Vision and Pattern Recognition (EMMCVPR), LNCS, vol. 2134, pp. 528–543.

Holloway, R.L., 1968. The evolution of the primate brain: some aspects of quantitative relations. Brain Res. 7, 121–172.

Holloway, R.L., 1992. The failure of the gyrification index (gi) to account for volumetric reorganization in the evolution of the human brain. J. Human Evol. 22, 163–170.

Holloway, R.L., 2002. Brief communication: how much larger is the relative volume of area10 of the prefrontal cortex in humans? Am. J. Phys. Anthropol. 118 (4), 399–401.

Holm, D.D., Ratnanather, J.T., Trouve, A., Younes, L., 2004. Soliton dynamics in computational anatomy. Neuroimage (Suppl. 1), S170–S178.

Huxley, T.H., Descent of Man, Charles Darwin, 1874. (Chapter: Note on the Resemblances and Differences in the Structure and the Development of the Brain in Man and Apes).

Joshi, S.C., Miller, M.I., 2000. Landmark matching via large deformation diffeomorphisms. IEEE Trans. Image Process. 9 (8), 1357–1370.

Joshi, S., Davis, B., Jomier, M., Gerig, G., 2004. Unbiased diffeomorphic atlas construction for computational anatomy. Neuroimage (Suppl. 1), S151–S160.

Marsden, J., Ratiu, T., 1999. Introduction to Mechanics and Symmetry. Springer Verlag, New York.

McBride, T., Arnold, S.E., Gur, R.C., 1999. A comparative volumetric analysis of the prefrontal cortex in human and baboon mri. Brain Behav. Evol. 54 (3), 159–166, 0006-8977 Journal Article.

Miller, M., 2004. Computational anatomy: Shape, growth and atrophy comparison via diffeomorphisms. Neuroimage (Suppl. 1), S19–S33.

Miller, M.I., Christensen, G.E., Amit, Y., Grenander, U., 1993. Mathematical textbook of deformable neuroanatomies. Proc. Natl. Acad. Sci. (USA) 90 (24), 11944–11948.

Miller, M., Trouve, A., Younes, L., 2002. On the metrics and euler-lagrange equations of computational anatomy. Annu. Rev. Biomed. Eng. 4, 375–405.

Miller, M.I., Trouve, A., Younes, L., 2003. Geodesic shooting for computational anatomy. Technical report, Center for Imaging Science, Johns Hopkins University.

Penfield, W., Rasmussen, T., 1950. Cerebral Cortex of Man, a Clinical Study of Localization of Function. Macmillan, New York.

Press, W.H., Teukolsky, S.A., Vetterling, W.T., Flannery, B.P., 2002. Numerical Recipes in C++, second ed. Cambridge University Press, Cambridge.

Rilling, J.K., Insel, T.R., 1999. The primate neocortex in comparative perspective using magnetic resonance imaging. J. Human Evol. 37, 191–223.

Schoenemann, P.T., Glotzer, L.D., 2003. Evolution of the prefrontal cortex: A stereological analysis of primate brain mri scans. Am. J. Phys. Anthropol. 120 (Suppl. 36), 185–186.

Schoenemann, P.T., Avants, B.B., Gee, J.C., Glotzer, L.D., Sheehan, M.J., 2004. Analysis of chimp–human brain differences via non-rigid deformation of 3d mr images. Am. J. Phys. Anthropol. 123, 174–175.

Semendeferi, K., Armstrong, E., Schleicher, A., Zilles, K., Van Hoesen, G.W., 1998. Limbic frontal cortex in hominoids: a comparative study of area 13. Am. J. Phys. Anthropol. 106 (2), 129–155.

Thompson, D.W., 1917. On Growth and Form. Cambridge University Press, England.

Thompson, P.M., Toga, A.W., 1998. Anatomically-driven strategies for high-dimensional brain image warping and pathology

detection. In: Toga, A.W. (Ed.), Brain Warping. Academic Press, San Diego, pp. 311–336.

Thompson, P.M., Mega, M.S., Toga, A.W., 1999. Disease-specific brain atlases. In: Mazziotta, J.C., Toga, A.W. (Eds.), Brain Mapping III: The Disorders. Academic Press, San Diego.

Tikhonov, A.N., Arsenin, V.A., 1977. Solutions of Ill-posed Problems. Winston, Washington, DC.

Trouve, A., 1998. Diffemorphism groups and pattern matching in image analysis. Intl. J. Comp. Vis. 28 (3), 213–221.

Twining, C., Marsland, S., 2003. Constructing diffeomorphic representations of non-rigid registrations of medical images. In: Taylor, C., Noble, J. (Eds.), Information Processing in Medical Imaging, LNCS vol. 2732. Springer Verlag, Ambleside, UK, pp. 413–425.

von Bonin, P.B.P.G., WS, G.W.S.M., 1950. The Isocortex of the Chimpanzee. University of Illinois Press, Urbana.

Yoo, T., 2003. Insight into Images: Principles and Practice for Segmentation, Registration and Image Analysis. AK Peters Ltd., Natick, MA.